A Step-Mountain Coordinate General Circulation Model: Description and Validation of Medium-Range Forecasts

B. L. WYMAN

Geophysical Fluid Dynamics Laboratory/NOAA, Princeton, New Jersey

(Manuscript received 9 January 1995, in final form 28 July 1995)

ABSTRACT

The step-mountain or eta vertical coordinate has been a proposed solution for eliminating the numerical errors encountered when calculating the pressure gradient force along sloping surfaces. The main objectives of this paper are to describe the development of a global general circulation model using the eta coordinate and to verify the capabilities of the model for medium-range forecasts. First, the treatment of the polar boundary and the polar filtering are presented. To verify the polar treatment, numerical results using the shallow-water equations are presented. Second, various physical parameterizations are incorporated into the multilevel eta coordinate model. Model integrations for several January cases are presented to validate the model.

The similarity of the eta coordinate formulation to the terrain-following sigma coordinate allows the model to be run using either vertical coordinate. Thus, model comparisons are performed with the eta and sigma coordinate versions of the general circulation model, keeping the same physical parameterizations. Additional comparisons are made with a sigma coordinate spectral model.

As a validation of the model, 10-day integrations are made from four observed initial conditions at several horizontal resolutions. At relatively low resolution, forecast results slightly favor the spectral and sigma coordinate models. However, at higher resolution, forecast skill scores for the eta coordinate model are indistinguishable from those of the sigma models. Additional results are presented to demonstrate the advantages of the eta coordinate near steep topography and the potential deficiency of the eta coordinate in connection with the surface boundary layer treatment.

1. Introduction

The terrain-following sigma vertical coordinate has been used widely in many numerical models since its introduction by Phillips (1957). The sigma coordinate is a modified version of the pressure coordinate with a formulation that is relatively uncomplicated. The terrain-following coordinate surfaces produce a lower boundary condition that is extremely simple. Alternative coordinate systems such as pressure or isentropic surfaces each have unique advantages. However, both of these coordinates are more complicated than the sigma system since their coordinate surfaces intersect the ground.

A troublesome problem with the sigma system (and most other terrain-following coordinates) is sloping coordinate surfaces over steep topography. In particular, numerical errors associated with the pressure gradient force have received considerable attention (Corby et al. 1972; Janjić 1977; Tomine and Abe 1982; Arakawa and Suarez 1983). Correction schemes developed to minimize these errors do not completely solve the problem. Regardless of the correction scheme, an increase in resolution may lead only to an increase in these errors. Increasing the horizontal resolution usually results in steeper mountains, and the combination of steeper mountains and thinner sigma layers may lead to larger pressure gradient force errors (Janjić 1977; Mesinger 1982).

The problem of steep mountains is not limited to the pressure gradient calculation; other horizontally differenced quantities reportedly show problems in regions of steep topography (Mesinger and Janjić 1987). The spurious horizontal diffusion of temperature or moisture along a sloping sigma surface may result in excessive precipitation in mountainous regions (Simmons and Jarraud 1984; Simmons 1987). For very steep sloping surfaces this may even lead to excessive noise and instability.

Motivated by the problems due to sloping sigma surfaces, Mesinger (1984) proposed an alternative vertical coordinate with fixed blocklike or step mountains. Mountains are represented as *filled* grid boxes, so that some grid boxes lie beneath the earth's surface and carry no data. The new coordinate surfaces remain nearly horizontal, eliminating many of the problems associated with the sigma system. The errors associated with the pressure gradient terms and other horizontally differenced quantities should be reduced. Yet, regard-

Corresponding author address: B. L. Wyman, Geophysical Fluid Dynamics Laboratory, Princeton University, P.O. Box 308, Princeton, NJ 08542.

less of the rather complex appearance of the lower boundary, the step-mountain coordinate remains relatively simple and similar to the sigma coordinate.

Equations defining the step-mountain vertical coordinate known as eta (η) and showing its relationship to the sigma (σ) coordinate are given below:

$$\eta \equiv \eta_s \sigma \tag{1a}$$

$$\sigma \equiv \frac{p}{p_s} \tag{1b}$$

$$\eta_s \equiv \frac{P_{\text{ref}}(z_s)}{P_{\text{ref}}(0)} . \tag{1c}$$

It is apparent from (1a) that the only modification needed to the sigma predictive equations is the incorporation of η_s, the value of eta at the earth's surface. In (1c) η_s is defined from a profile of reference pressures P_{ref} located at the interface between model layers. The surface height z_s is chosen from a set of reference heights located at these model layer interfaces, so that the model topography will have a steplike structure.

Because of the eta coordinate's close similarity to the sigma coordinate, some unique advantages occur. Using the relationship in (1a) and a masking array for the step mountains, the same computer code may be used to run with either an eta or sigma coordinate model. Thus, intercomparisons between coordinates can be made without concern for potential computer coding errors. Furthermore, in the absence of topography ($z_s = 0$), the eta coordinate is identical to the sigma coordinate (i.e., $\eta_s = 1$).

Although the eta coordinate virtually eliminates the errors due to sloping coordinate surfaces, new potential problems might arise due to the loss of vertical resolution near the earth's surface above elevated terrain. Higher vertical resolution is typically placed in the lowest sigma layers to handle the calculation of surface fluxes. With the eta coordinate, the lowest model layers would be filled with blocklike mountains, and the model level closest to the surface will have a coarser resolution and may be too deep a layer to correctly compute the surface fluxes. Thus, the choice of a surface-layer turbulence scheme and the vertical resolution in the lower troposphere are important issues to consider.

A global gridpoint model has been in development at the Geophysical Fluid Dynamics Laboratory (GFDL) for many years (Mesinger 1981), but the particular version presented in this paper has evolved from the National Meteorological Center (NMC) regional eta model (Mesinger et al. 1988, hereafter M88; Janjić 1990). Boundary conditions have been applied for the global domain, and the physical parameterizations have been modified to be consistent with the E4 physics package of the GFDL Experimental Prediction Group spectral model (Gordon and Stern 1982). The general circulation model (GCM) described in this paper will be referred to as the global eta model (GEM). Currently this is the only known application of the eta coordinate in a global model.

The goal of the work presented in this paper has been to develop a global hydrostatic gridpoint model, using state-of-the-art numerical techniques, applicable for medium- and extended-range weather prediction. This paper's definition of medium-range forecasts will be out to 10 days. Extended-range predictions with 1–3-month timescales will be discussed in a later paper. The effect of the eta coordinate on the atmospheric general circulation for these longer timescales has never been determined. With the recent success of the regional NMC eta model (Mesinger and Black 1992), it will be interesting to examine the merit of the eta coordinate within the global domain.

The horizontal grid and numerical schemes used in the polar region will be presented in section 2. An appendix presents integrations with the shallow-water equations demonstrating that cross-polar flow is handled adequately with little distortion. Section 3 will describe the three-dimensional version of the model with full physics for use as a GCM. This will include a description on how the model's geography was generated and a summary of the model's dynamics and physical parameterizations. An emphasis will be given to differences from the NMC eta model and the E4 physics package. Section 4 will provide a validation of the model from four test cases of 10-day model runs. The sigma coordinate version will be compared to the spectral model, the eta coordinate version will be compared to the sigma version, and differences in forecast skill will be discussed. In addition, the eta coordinate's advantages over steep topography and disadvantages near the earth's surface will be examined. Concluding comments are provided in section 5.

2. The horizontal grid and polar treatment

a. The horizontal grid

The GEM uses the semistaggered Arakawa E grid (Arakawa and Lamb 1977; Janjić and Mesinger 1984). The arrangement of variables on this grid is shown in Fig. 1. Referring to the figure, the wind components along the λ and φ axes (denoted by the circled letters u and v, respectively) are defined at one set of grid points called velocity points, while all other variables are carried at another set of grid points referred to as mass points (denoted with the boxed letter h). The latitudinal and longitudinal grid spacing, $\Delta\varphi$ and $\Delta\lambda$, respectively, is the distance between neighboring mass and velocity points along the φ and λ axis. The nearest neighboring grid point of the same type is located along a diagonal axis at a distance d. These diagonal axes shall be referred to as the λ' and φ' axes. In the local coordinate system on the sphere the λ and φ axes correspond to the x and y axes, respectively.

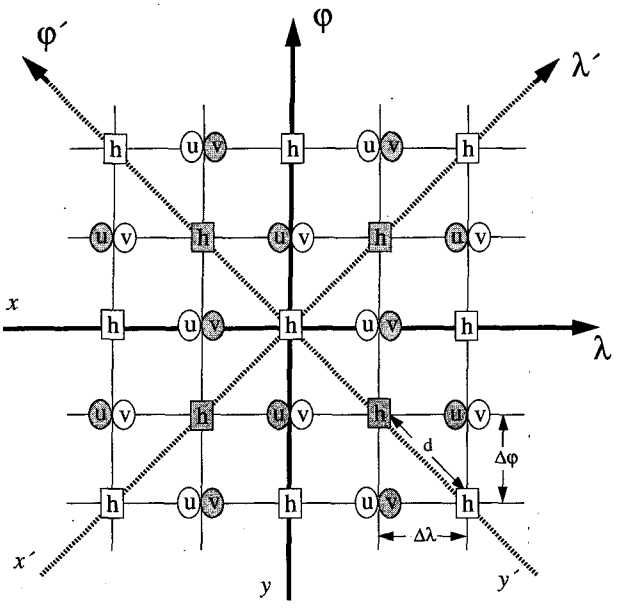

FIG. 1. The semistaggered Arakawa E-grid configuration.

The current horizontal resolutions used by the GEM are denoted as E45 and E60. The number following the "E" designates the number of latitude rows in the global E grid between the equator and pole. For the E45 resolution, $\Delta\varphi$ equals 2.0° and $\Delta\lambda$ equals 3.0°, and for the E60 resolution, $\Delta\varphi$ and $\Delta\lambda$ equal 1.50° and 2.25°, respectively.

b. The polar region

The polar boundary condition adopted for the GEM was proposed by Rančić and Ničković (1988) for the shallow-water equations on the global E grid. Although their scheme was designed to conserve globally averaged mass and total energy, minor modifications were required to the scheme in the vicinity of the pole to guarantee that there was no distortion of cross-polar flow. Namely, when computing the momentum advection at the latitude row adjacent to the pole only momentum fluxes in the latitude and longitude directions were used. The momentum fluxes along the diagonal axes were eliminated. In addition, the mean polar height was used for all calculations rather than carrying a height at each grid point along the polar line. Several test cases are presented in the appendix to verify uniform flow across the pole.

Referring to Fig. 1, the Arakawa E grid can be decomposed into two overlapping fully staggered C grids. These two C grids are depicted by the shaded and unshaded rectangles and circles. If only the inertial–gravity terms are considered, the large-scale solution of each of these C grids can exist independently and will diverge from one another. This causes two-grid-interval noise in the E-grid solution. Mesinger's (1973) modification to the continuity equation is used to avoid this difficulty. This modification is added into the equation for mass divergence (and subsequently the surface pressure tendency) in the form described by M88 [their Eq. (4.5)]. The application of this scheme with the shallow-water equations on the global grid revealed this term to be very unstable near the pole. To suppress this instability the modification term was multiplied by a damping factor with the form

$$D_c = \frac{(\cos\varphi_j)^2}{(\cos\varphi_c)^2}, \tag{2}$$

where $0 \leq D_c \leq 1$, φ_c is the latitude at which the damping begins and φ_j is the latitude for row j (the meridional index). As φ_c is decreased, damping applied to the divergence modification term near the pole increases. Implementation of the modification scheme to the global grid has required several tests to determine optimal values; $w = 0.15$ and $\varphi_c = 76°$ are used by the GCM, where w is the weighting factor of the modification (Janjić 1979; Janjić et al. 1988).

A polar filtering scheme is used to damp the shortest resolvable waves so that a longer time step can be taken. The filtering technique used is analogous to the time tendency filter (scheme c) used by Takacs and Balgovind (1983). This filtering scheme does not necessarily conserve energy. Filtering is done poleward of 60° latitude and is applied to time tendencies of horizontal advection and the adjustment terms. The adjustment terms include the pressure gradient force, Coriolis and curvature terms, divergence, and the horizontal part of the omega-alpha equation (in the GCM). The fields are filtered by transforming a full latitude circle of data into its Fourier components using a fast Fourier transform (FFT). The Fourier components are damped (i.e., multiplied) by a given function of wavenumber and latitude and then transformed back to gridpoint space using the inverse FFT. The polar filter function used for damping the Fourier components was determined in a manner similar to Takacs and Balgovind (1983); it is related to wavenumber k and latitude row j and is defined as

$$S_j(k) = \sqrt{2}\,\frac{\cos\varphi_j}{\cos\varphi_{\text{ref}}}\left[(\sin X)^2 + \frac{1}{2}(\cos X - 1)^2\right]^{1/2} \tag{3}$$

where $0 \leq S_j(k) \leq 1$, $X = 2k\Delta\lambda$ and φ_{ref} is the reference latitude (60°) poleward of which filtering is performed (F. Mesinger and M. Rančić 1986, personal communication). The strength of the filter increases with higher wavenumbers and latitude. The use of the polar filter with the step-mountain coordinate will be discussed in section 3.

3. General circulation model

a. The vertical coordinate

Although the formulation of the eta or step-mountain coordinate is similar to that of the sigma coordinate,

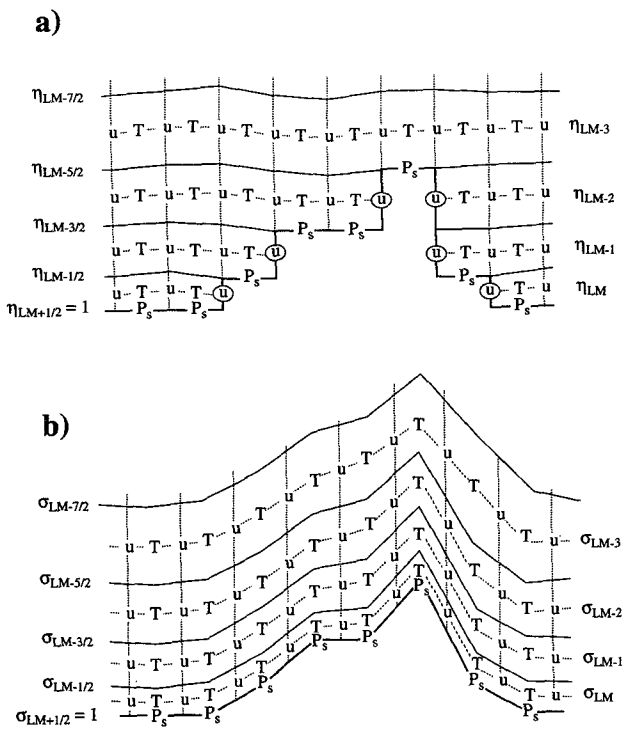

FIG. 2. Cross sections in the $x-z$ plane depicting (a) the eta coordinate (after Mesinger et al. 1988) and (b) the sigma coordinate. Both cross sections have identical heights at each grid point in the x direction. The circled letter u in (a) represents internal boundary points where the velocity is set to zero.

the physical features are quite different. Figure 2 depicts a cross section view along the $x-z$ plane of the eta coordinate (top panel) and sigma coordinate (bottom panel) for identical mountains. In the bottom panel, the difficulty in accurately computing horizontally differenced quantities along the sloping sigma surfaces is obvious. The eta coordinate with its relatively flat surfaces avoids this difficulty but introduces some new concerns due to the loss of vertical resolution near the earth's surface.

The lower boundary of the eta coordinate contains so-called internal boundaries (see M88), which occur where the free atmosphere intersects the vertical walls of the step mountain. In Fig. 2 the internal boundaries are denoted by the circled u. These boundaries occur only at velocity points and the velocity components are set to zero. The velocity points underground are also set to zero. All conserved quantities of the original numerical schemes are still conserved for the eta coordinate internal boundaries with the exception of momentum. M88 found no adverse effects caused by the lack of momentum conservation or internal boundaries, and the GEM has not shown any problems related to this either.

The current version of the GEM uses 18 vertical levels denoted by the notation L18. The placement of these levels is shown in Fig. 3. The model levels (indicated by dashed lines) are located at the midpoint of a model layer. The prognostic variables temperature, specific humidity, and the horizontal wind components are carried at the model levels, while vertical velocity ($\dot{\eta}$) is carried at the interface between layers. Note that for the eta coordinate, at grid points having some elevation (i.e., step topography) the number of levels will be less than 18. The boundary condition at the top of the model is $\dot{\eta} = 0$ and at the step-mountain surface (regardless of the height of the topography) is $\dot{\eta}_s = 0$.

Although the eta coordinate should eliminate most of the problems associated with sloping coordinate surfaces, the loss of vertical resolution in the lower troposphere may lead to several additional problems. In many numerical models, a relatively higher vertical resolution is used in the lower troposphere to help resolve the surface fluxes and simulate the surface boundary layer. For example, the sigma version of this model has a depth in the layer between the earth's surface and the lowest atmospheric level of about 35 m. With the height of most land areas on the order of several hundreds of meters, a comparable resolution for the surface layer at all eta coordinate grid points would require

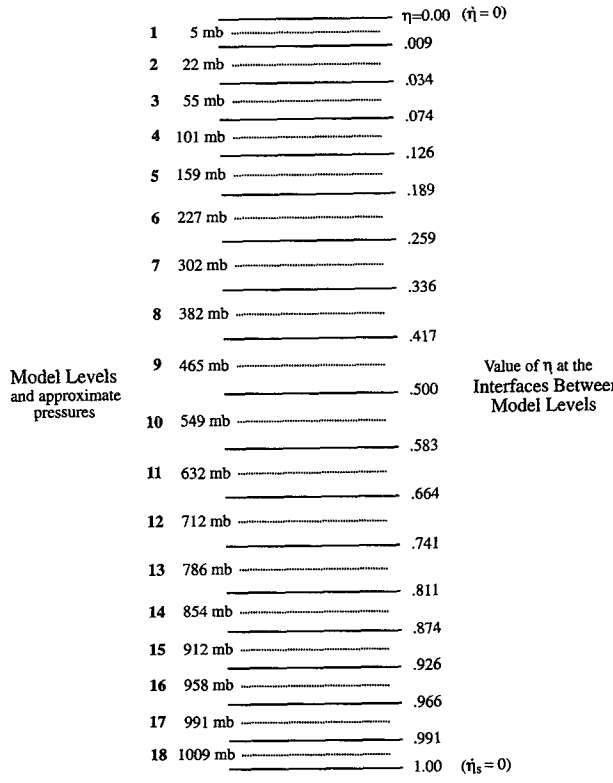

FIG. 3. Structure of the 18-level vertical grid (not drawn to scale). Model levels are indicated by dashed lines and the interfaces between levels are solid lines. Approximate model level pressures assume a sea level reference pressure of 1013.25 mb.

many more vertical levels than currently used. Another less obvious problem occurs where the earth's true topography gradually slopes over a large distance, such as over the Great Plains in North America. A geographic feature like this would be represented in the eta coordinate by several long, flat plains. For the first of these problems, the choice of a surface-layer turbulence scheme can be very important. An increase in vertical and horizontal resolution would certainly help to minimize both of these problems.

The eta coordinate presents some problems for the polar filtering scheme described in section 2. The problem occurs when a latitude circle of grid points that should be filtered does not lie entirely above (or below) the step mountain. The FFT expects a 360° latitude circle of equally spaced data points. The GEM uses a simple approach of first linearly interpolating data to the underground points from adjacent aboveground points. Next, polar filtering is performed as described in section 2 for the full latitude circle of points. Finally, a check is made on the aboveground data points to guarantee that the zonal mean of the original unfiltered data has not been changed during the filtering. Any difference in the zonal mean before and after filtering is distributed equally among all aboveground points in the given latitude circle and at the same model level.

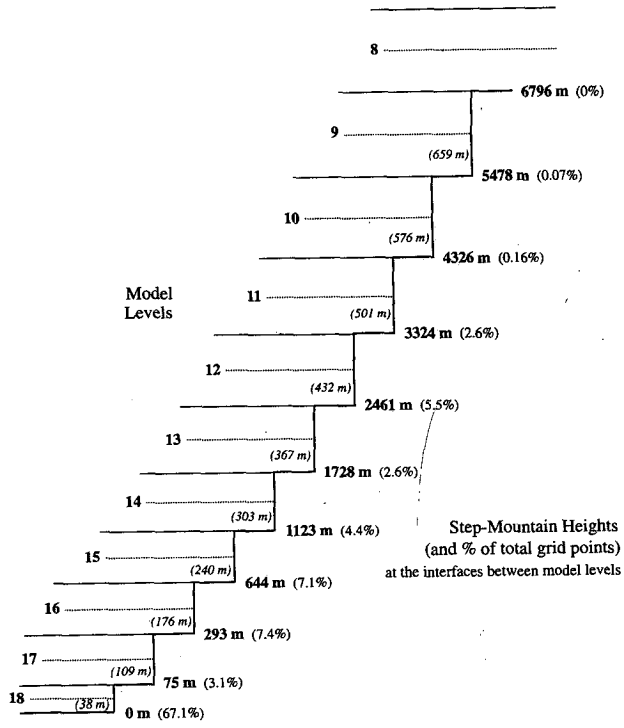

FIG. 4. Depiction of the profile of step-mountain heights corresponding to eta values at model layer interfaces in Fig. 3. The average surface-layer depth and percentage of grid points at each step is in parentheses.

b. *Discretization of topography and land–sea mask*

The topography surfaces of the eta coordinate lie at the interface between model layers. The discretization process sets the terrain height of a grid box to a height in a predefined reference profile. This reference profile of height as a function of η is defined

$$z_\eta = \frac{T_{\text{ref}}}{\gamma_{\text{ref}}}(1-\eta)^{R\gamma_{\text{ref}}/g}. \qquad (4)$$

A reference temperature $T_{\text{ref}} = 288$ K at sea level (i.e., $\eta = 1$) and a constant lapse $\gamma_{\text{ref}} = 6.5 \times 10^{-3}$ K m^{-1} are assumed. The gas constant for dry air is R, and the gravitational constant is g. For the vertical structure in Fig. 3, the resulting profile of step-mountain heights is depicted in Fig. 4. All grid boxes will have a surface height corresponding to a height in Fig. 4. Approximate depths of the surface layer at each step height is given in parentheses to illustrate the eta coordinate's potential difficulty encountered in this layer.

Of concern in the discretization of the topography is the creation of grid boxes, in which the horizontal differencing schemes have no effect. This problem occurs at a height point when the four surrounding velocity points are internal boundary points (i.e., velocities set to zero); M88 has named these "isolated valleys." This model removes the isolated valleys using the four-point silhouette averaging technique (M88). Four-point mountains are formed by averaging the heights at four adjacent grid boxes (see M88 Fig. 3). The silhouette averaging technique attempts to retain some of the barrier effects of the original topography. M88 uses this four-point silhouette averaging technique over the entire domain (except near boundaries)[1]; however, at the relatively coarse resolution of the global model the four-point silhouette mountain creates a substantial loss in geographical detail. Therefore, it was desirable to use the four-point technique only at grid boxes where isolated valleys occur, so that the global model's topography would consist of a mix of single-point and four-point silhouette mountains.

A global land–sea mask was created from the percent water coverage in each grid box. The land–sea mask for a single grid box was determined solely by this percentage. If a four-point mountain was created, as described above, a coinciding four-point land–sea box was also created. Four-point boxes were considered ocean (land) boxes when three or four single boxes were ocean (land). If two single boxes are defined as sea and two as land, then the average percent-

[1] At the time this paper is written, the current version of the NMC eta model uses only single-point mountains and removes the isolated valleys by increasing their height (F. Mesinger 1993, personal communication).

age of the entire four-point box was used to determine the land–sea mask.

Whenever a sea point exists, for either a single-point grid box or a four-point grid box, the geopotential height is set to zero. This has been done to accommodate the prescribed sea surface temperatures. If the ocean surface was allowed to be above sea level, then an adjustment of the sea surface temperatures would be required.

Global U.S. Navy datasets of mean topography and percent water for a $1/6^\circ$ grid were used to create the model topography and land–sea mask. Spatial averaging was used to convert these fields to the appropriate E-grid resolution. Polar filtering was applied to the fields on the E grid prior to the discretization process to remove any small-scale noise that might potentially create an instability in high latitudes. The fields were converted to step mountains by choosing the closest step height from the reference profile depicted in Fig. 4. The percentage of grid points occurring at each step height at the E45 resolution is denoted in Fig. 4 after the corresponding height. Similar percentages occur at the E60 resolution.

Despite the use of single-point mountains and silhouette mountains the model topography underestimates the true topography. For instance, the Himalayas at 5478 m have a maximum height less than what might be expected for the horizontal resolution used. If they were represented by one additional step, they would be too high (6796 m). To improve the representation of the eta coordinate step topography, an increase in vertical resolution (especially in the lower troposphere) would be advantageous.

c. The basic equations

The fundamental quantities predicted by the model are the x and y components of the wind, temperature, specific humidity, and surface pressure. The governing equations written for the eta coordinate version follow that of M88 and Mesinger (1984). The prognostic equations for momentum (u and v), temperature (T), and specific humidity (q) can be written as

$$\frac{d\mathbf{v}}{dt} + f\mathbf{k} \times \mathbf{v} + \nabla\Phi + \frac{RT_v}{p}\nabla p + \mathbf{F} = 0 \quad (5a)$$

$$\frac{dT}{dt} + \frac{1}{c_p}\frac{RT_v}{p}\left[\int_0^\eta \left(\nabla\cdot\frac{\partial p}{\partial \eta}\mathbf{v}\right)d\eta - (\mathbf{v}\cdot\nabla p)\right] + T_R + T_C + F_T = 0 \quad (5b)$$

$$\frac{dq}{dt} + Q_C + F_Q = 0. \quad (5c)$$

The continuity equation is given as

$$\frac{\partial}{\partial \eta}\left(\frac{\partial p}{\partial t}\right) + \nabla\cdot\left(\mathbf{v}\frac{\partial p}{\partial \eta}\right) + \frac{\partial}{\partial \eta}\left(\dot{\eta}\frac{\partial p}{\partial \eta}\right) = 0. \quad (6)$$

The vertical velocity $\dot{\eta}$ is computed from

$$\dot{\eta}\frac{\partial p}{\partial \eta} = -\frac{\partial p}{\partial t} - \int_0^\eta \left(\nabla\cdot\mathbf{v}\frac{\partial p}{\partial \eta}\right)d\eta, \quad (7)$$

and the surface pressure p_s tendency is computed from

$$\frac{\partial p_s}{\partial t} = -\int_0^{\eta_s}\left(\nabla\cdot\frac{\partial p}{\partial \eta}\mathbf{v}\right)d\eta. \quad (8)$$

Geopotential height Φ is determined from the hydrostatic equation

$$\frac{\partial \Phi}{\partial \eta} = -\frac{RT_v}{p}\frac{\partial p}{\partial \eta}, \quad (9)$$

where R is the gas constant for dry air, T_v is the virtual temperature, and p represents pressure.

Note that the divergence modification, although not included in these equations, is applied to the horizontal part of (6) and therefore is also included in the vertical integral of mass divergence in (5b), (7), and (8). The Coriolis and curvature terms in (5a) are defined as $f = 2\Omega\sin\varphi + ua^{-1}\tan\varphi$, where a and Ω are the radius and angular speed of rotation of the earth, respectively; $\mathbf{F}$, F_T, and F_Q represent the diffusion terms of momentum, temperature, and specific humidity, respectively; T_C and Q_C are the rates of convective heating and convective condensation of water vapor, respectively; and T_R is the rate of radiative temperature change. The virtual temperature is determined from

$$T_v = T(1 + 0.608q). \quad (10)$$

d. The dynamics

The model is integrated using an additive split time differencing (Gadd 1978) so that a longer advective time step could be taken. The advective time step was always four times that used for the adjustment processes. The adjustment time step was 240 and 120 s for the E45 and E60 models, respectively. In addition, the forward–backward scheme is applied to the adjustment terms along with the trapezoidal implicit scheme for the Coriolis terms (Mesinger 1977; Janjić 1979).

Vertical advection of temperature, momentum, and turbulent kinetic energy (TKE, to be described later) are calculated using centered spatial differencing, while specific humidity uses an upstream differencing technique. All variables use an Euler-backward time-differencing scheme (Kurihara 1965; Matsuno 1966). Negative specific humidities generated by vertical advection are corrected by borrowing from the layer below.

Horizontal advection is performed using the Janjić (1984) second-order nonlinear advection scheme. The scheme is designed from the Arakawa Jacobian that conserves both energy and enstrophy as defined on the C grid (Arakawa 1966; Arakawa and Lamb 1977). Time differencing is performed with a modified Euler–backward scheme that has considerably less damping than the standard scheme (F. Mesinger 1988, personal communication; also see Kurihara and Tripoli, 1976). Following horizontal advection, negative specific humidities (and negative TKE) are corrected by borrowing from neighboring grid points having positive values. If negative values remain after two passes through this scheme, they are allowed to remain.

e. The physical parameterizations

The model uses the so-called E4 physical parameterizations (Miyakoda and Sirutis 1977; Sirutis and Miyakoda 1990). Distinguishing features of these parameterizations include the turbulence closure scheme, the surface-layer interface, and the subsurface heat exchange. Many of the parameterizations were originally applied using the sigma coordinate but have been adapted to the eta coordinate. An emphasis will be placed on describing the conversion to the eta system. A summary of the model's physical packages with appropriate references is given in Table 1.

1) RADIATION AND CONVECTION

The Fels and Schwarzkopf radiative scheme (Fels and Schwarzkopf 1975; Fels and Schwarzkopf 1981; Schwarzkopf and Fels 1991) has been incorporated into the GEM. Several modifications to the shortwave and longwave algorithms were required so that the varying number of vertical levels in the eta system would give accurate heating rates and surface fluxes. A verification of the accuracy of the modifications was made by running in a *clear-sky mode* (without clouds, water vapor, or ozone); differences between the eta and sigma solutions were found to be minimal.

The model employs seasonally varying radiation with no diurnal variability; radiative tendencies are updated every 12 h. Seasonally varying zonal clouds and ozone are prescribed. To avoid systematic differences over topography, the clouds and ozone are interpolated to approximately the same pressure level for both the eta and sigma versions of the model.

The moist convective adjustment process uses the schemes described by Manabe et al. (1965). The criterion for saturation was set at 100% relative humidity. Condensed water falls out directly as precipitation; it is not allowed to evaporate in dry layers below. The temperature and specific humidity fields are adjusted on the advective timescale (every fourth time step) for the amount of water vapor condensed.

2) LATERAL DIFFUSION

Nonlinear fourth-order lateral diffusion is applied explicitly on the adjustment time step to the temperature, specific humidity, turbulent kinetic energy, and momentum fields. The fourth-order scheme provides a more scale-selective dissipation than second-order schemes where the synoptic scales may be damped too

TABLE 1. Summary of physical parameterizations.

Parameterization	Package description and comments	Reference
Radiation	Fels–Schwarzkopf • prescribed seasonally varying zonal clouds and ozone • tendencies updated every 12 h	Fels and Schwarzkopf (1975) Fels and Schwarzkopf (1981) Schwarzkopf and Fels (1991)
Turbulence closure (vertical mixing coefficient)	Mellor–Yamada 2.5	Janjić (1990) Mellor and Yamada (1982)
Surface-layer mixing	Monin–Obukhov similarity theory	Delsol, et al. (1971)
Convection and large-scale condensation	Moist convective adjustment • 100% condensation criteria	Manabe et al. (1965)
Gravity wave mountain drag	Pierrehumbert	Pierrehumbert (1987)
Horizontal diffusion	Fourth order, nonlinear	Janjić (1990) Smagorinsky (1963)
Surface temperature prediction	Prognostic heat balance equation • three subsurface soil layers	Deardorff (1978)
Hydrology • soil moisture • snow cover	Single bucket method • 150-mm capacity everywhere Predicted snow cover	Manabe (1969)
Additional damping	Newtonian damping • at top two model levels	
Time differencing	Split explicit • for all physics, except Implicit • for vertical diffusion	Gadd (1978)

much. Nonlinear second-order mixing is computed along the x' and y' axes in a fashion similar to Smagorinsky (1963) and then reapplied to achieve an equivalent nonlinear fourth-order diffusion (Janjić 1990). The following equation expresses this relationship for any variable α:

$$\left(\frac{\partial \alpha}{\partial t}\right)_{HDIFF} = K_{\nabla^4}\nabla^4\alpha \approx K_{\nabla^2}\nabla^2(\Delta t K_{\nabla^2}\nabla^2\alpha). \quad (11)$$

The second-order operator for a variable α located at mass points is computed as

$$K_{\nabla^2}\nabla^2\alpha = \left(\frac{k_0 d_{\min}^2}{S_j}\right) \times \frac{1}{p}\left\{\frac{\partial}{\partial x'}\left[C_{x'}\overline{|D|}^{x'}\overline{S_j}^{x'}\overline{p}^{x'}\frac{\partial}{\partial x'}(\alpha)\right] + \frac{\partial}{\partial y'}\left[C_{y'}\overline{|D|}^{y'}\overline{S_j}^{y'}\overline{p}^{y'}\frac{\partial}{\partial y'}(\alpha)\right]\right\}, \quad (12a)$$

where α is either temperature, specific humidity, or turbulent kinetic energy. Similarly, the second-order operator for momentum is

$$K_{\nabla^2}\nabla^2\mathbf{v} = \left(\frac{k_0 d_{\min}^2}{S_j}\right)\left\{\frac{\partial}{\partial x'}\left[C_{x'}\overline{|D|}^{y'}\overline{S_j}^{x'}\frac{\partial}{\partial x'}(\mathbf{v})\right] + \frac{\partial}{\partial y'}\left[C_{y'}\overline{|D|}^{x'}\overline{S_j}^{y'}\frac{\partial}{\partial y'}(\mathbf{v})\right]\right\}. \quad (12b)$$

Deformation is defined at mass points as $|D| = (D_T^2 + D_S^2)^{1/2}$, where $D_T = \partial u/\partial x - \partial v/\partial y$ and $D_S = \partial v/\partial x + \partial u/\partial y$. The area of a grid box is defined $S_j = 4\Delta x_j \Delta y$, $d_{\min}$ is the minimum grid distance along the diagonal axis, the variables at mass points are weighted by pressure p, and k_0 is a user-specified constant mixing coefficient. Note that k_0 does not have the same meaning as k_0 in the second-order Smagorinsky diffusion scheme. The overbar represents the simplest two-point average along the specified axis.

The dimensionless correction factors $C_{x'}$ and $C_{y'}$ are designed to reduce excessive diffusion due to sloping sigma surfaces:

$$C_s = \left(1 + \frac{c_0}{c_p}|\Delta_s\phi|\right)^{-1}, \quad (13)$$

where s represents the x' or y' axis, c_p is the specific heat capacity, c_0 is a specified constant, and $\Delta_s\phi$ is the geopotential height difference between adjacent grid points in the finite-difference Laplacian. As the slope ($\Delta_s\phi$) between adjacent grid points increases, the correction factor (and diffusion) decreases. Although this slope correction does not substantially affect the eta coordinate diffusion, it was used for both vertical coordinates to provide a more equal comparison.

The nonlinearity of the scheme arises from the inclusion of the deformation term. The deformation varies considerably within the model's domain in a systematic manner. Spurious large deformations can be found in polar regions, because Δx becomes small, and large values also occur at the top of the model, where the magnitude of the wind is larger. In both of these regions, stronger diffusion would be desirable. When the deformation becomes too large the diffusion scheme becomes unstable; for this reason deformations are limited to $|D|_{\max} = (8k_0\Delta t)^{-1}$. This upper limit was derived from stability criteria for the five-point Shapiro filter (Shapiro 1970).

For comparison with other models the fourth-order diffusion coefficient can be expressed as $K_{\nabla^4} \approx (k_0 d_{\min}^2 |D|)^2 \Delta t$. Currently, for all resolutions of the model $k_0 = 5.0$. Assuming a global average deformation (i.e., $|D| = 3 \times 10^{-5}\ s^{-1}$), the resulting fourth-order diffusion coefficient for the E45 model ($K_{\nabla^4} = 1.3 \times 10^{16}\ m^4\ s^{-1}$) and the E60 model ($K_{\nabla^4} = 2.1 \times 10^{15}\ m^4\ s^{-1}$) are comparable to other global models (Gordon and Stern 1984; Simmons and Jarraud 1984; Simmons 1988). Using these average diffusion coefficients, damping (e folding) times for a typical synoptic-scale wave (1000 km wavelength) would be 0.57 and 3.5 days for the E45 and E60 models, respectively. Alternatively, damping of the shortest resolvable waves at 45° latitude would have an e-folding time of 1.4 and 2.7 h, respectively, for the two models.

3) VERTICAL DIFFUSION

Vertical diffusion is performed on the advective time step to momentum, (virtual potential) temperature, specific humidity, and TKE. For the exchange between model levels in the free atmosphere, mixing coefficients are computed within the framework of the Mellor–Yamada level 2.5 turbulence closure scheme (Mellor and Yamada 1982). Vertical mixing between the model's bottom level and the earth's surface is handled with Monin–Obukhov theory. The GEM does not include the viscous sublayer as described by Janjić (1990).

This model's implementation of the Mellor–Yamada level 2.5 scheme follows that of Janjić (1990), with the exception of several changes that were made so that the vertical diffusion parameterization would conform with the E4 physics. These changes include the following. 1) The mixing coefficients are allowed to range up to $10^4\ m^2\ s^{-1}$. 2) Constraints on the auxiliary stability functions G_M and G_H, given by Eq. (3.9) in Janjić (1990), were changed back to the original constraints in Mellor and Yamada (1982). 3) The set of equations representing the exchange of a given quantity for all model levels is solved implicitly. The model deviates from the E4 physics by including the advection term for TKE, computed in the same fashion as Janjić (1990). This is considered a minor difference

from the E4 physics since the contribution of the advection term is relatively small when compared to the production/dissipation term for TKE.

Exchange coefficients defining the vertical mixing between the model's lowest level and the earth's surface are determined from Monin–Obukhov similarity theory (Delsol et al. 1971). The surface layer formally extends from a height z_0 just above the earth's surface upward to a height z, the top of the so-called constant flux layer. The roughness length z_0 is computed with the Charnock formula over oceans and is set to 0.1682 m over all land areas. The top of the constant flux layer z is determined by hydrostatically calculating the height from the lowest model level to the earth's surface. For the sigma version, this layer has a depth on average of about 35 m. Over the higher step-mountain surfaces of the eta coordinate, the depth of this layer will be on the order of several hundred meters. The use of a surface layer turbulence scheme for a layer of this depth is obviously questionable. However, the usefulness of these schemes may not be completely lost for modeling the general circulation. Techniques necessary to improve the validity of the calculation of turbulent fluxes may require extensive efforts and is not the primary goal of the present study. Therefore, the GEM uses a straightforward approach with the Monin–Obukhov scheme by simply adjusting the depth of the constant flux layer. The impact of this technique on the magnitude of the surface fluxes will be examined in section 4.

When computing surface fluxes and vertical shears there is the need for the wind velocity at height points. For a sigma coordinate model on the E grid, the usual technique is to average the four surrounding velocities to the height point. However, because of the internal boundaries, the eta coordinate does not always have four velocities adjacent to a height point. In this case the average will be taken with the available surrounding velocities. With the algorithm for determining the step mountains there will be at least one velocity surrounding each mass point.

4) Surface processes

The model predicts the surface temperature in a thin layer of soil at land points and at sea-ice points, while the temperature of the open ocean surface is specified. To conform with the E4 physics, the model has three additional subsurface soil layers, the temperature of the two uppermost layers is predicted while the lowest layer remains fixed. The vertical structure (i.e., depth) of the subsurface soil layers is identical to those of Miyakoda and Sirutis (1977).

When the model is initially started, a straightforward heat balance is performed, for which the time derivative of surface temperature and the soil heat conduction are set to zero. At all subsequent model time steps, prognostic equations for the surface heat balance and heat exchange between soil layers are solved simultaneously. The change in surface temperature due to melting snow cover is solved as a separate step, and the melted snow is added to the soil moisture content.

Soil moisture content is determined by the single bucket method (Manabe 1969). The maximum allowable depth per grid box is 0.15 m over the entire domain. The soil moisture cannot exceed 0.15 m; any excess is considered runoff and disappears from the model. The soil moisture content impacts the evaporation rate over land.

Depth of water equivalent snow cover is a predicted quantity over land points only; sea and sea-ice points do not accumulate snow. When precipitation occurs, it is considered to fall as snow if the surface temperature is below freezing. The depth of the snow modifies the albedo of the land surface. Albedos over the ocean and sea ice are predetermined functions of latitude and zenith angle of the sun.

5) Gravity wave drag and Newtonian damping

Neither gravity wave drag nor Newtonian damping are considered part of the E4 physics package but have been adapted to this model with the primary purpose of keeping the physical parameterizations similar to those of the GFDL Experimental Prediction Group spectral model.

Gravity wave drag due to subgrid-scale topography has been parameterized using the scheme described by Pierrehumbert (1987). A base momentum flux is determined in a layer near the earth's surface. This base flux is then redistributed in the middle and upper atmosphere by applying a stress on the horizontal momentum components where areas of wave breaking are identified. Stern and Pierrehumbert (1988) define this *low-level layer* near the earth's surface by the lowest 6 levels of their 18-level sigma model. In the 18-level sigma version of the GEM, the lowest 6 levels represents about 22% of the atmosphere. Since the eta coordinate has a varying number of levels, the *low-level layer* is defined by the number of model layers that is closest to this 22% proportion of the atmosphere; however, there must be at least two levels.

A Newtonian-type damping of the temperature field is done at the two uppermost levels of the model. Although, both the GEM sigma and eta coordinates have a cold bias in the stratosphere, and Newtonian damping helps to alleviate some of this, the damping is not needed for the stability. The zonal mean temperature of the model is damped toward a climatological zonal mean temperature. The climatological temperatures and the strength of the damping were chosen for agreement with the spectral model. The uppermost model level uses a damping time of 25 days, and the level below uses 50 days.

4. Model Integrations

a. Experimental design

Model integrations have been run with the GEM using both the sigma and eta coordinates. Parallel integrations were made with a T30 version of the spectral transform model (Gordon and Stern 1982), which uses the sigma coordinate. All models used the E4 physical parameterizations. The spectral model has been used extensively by the Experimental Prediction Group at GFDL for other research activities. In the present study, the intent of the spectral model integrations is for purposes of reference since a detailed comparison of gridpoint versus spectral differences would be quite involved and beyond the scope of this work.

The GEM was run at horizontal resolutions of E45 and E60. The E45 resolution with 5342 grid points per horizontal level has a resolution close to the T30 model's Gaussian grid of 96 × 48, or 4608 grid points per level. The E60 resolution has a considerably finer resolution with 9522 points per level. All models used 18 levels in the vertical with the placement of the levels nearly identical (see Fig. 3).

The parameterizations for moist convection, radiation, gravity wave drag, and Newtonian damping have been developed from the same algorithms, so that minimal differences exist between the spectral and gridpoint models. The most significant differences occur in the lateral diffusion schemes. Both models have fourth-order lateral diffusion; however, the gridpoint models use a nonlinear deformation term and the spectral model uses linear diffusion. The effect of these differences has not been investigated. In addition, spectral truncation has created differences between spectral and gridpoint fields, such as topography, that cannot be avoided.

To minimize differences between the GEM sigma and eta coordinate, both models use the same topography and land–sea mask at all grid points. By using identical geography for both coordinates, a direct comparison can be made of quantities at or near the surface. In particular, the surface fluxes, wind stress, and surface temperature should not display large systematic differences between the vertical coordinates. This would guarantee that the lowest atmospheric model level of both coordinates is influenced similarly by the underlying surface.

To evaluate the performance of the models, 10-day integrations were made for four January cases. The initial conditions were at 0000 UTC 1 January for the years 1979, 1980, 1981, and 1983. For all models, initial model data were created from identical sources. The primary three-dimensional model variables were interpolated from NMC level III analyses. Observed sea surface temperatures were specified from the AMIP (Atmospheric Model Intercomparison Project) dataset (Gates 1992). Initial snow cover and soil moisture fields were determined from the ECMWF (European Centre for Medium-Range Weather Forecasts) January climatology. The snow-free surface albedos over land were derived from CLIMAP (climate: long-range investigation, mapping and prediction) data.

b. Model validation

Figure 5 shows a Northern Hemisphere polar stereographic projection of 500-mb height used for the initial condition at 0000 UTC 1 January 1979. Similarly mapped in Fig. 6 and Fig. 7 for forecasts of 5 days and 10 days, respectively, are the spectral model forecast (lower left) and E45 GEM forecasts using the sigma coordinate (upper right) and eta coordinate (lower right). The verifying analysis (NMC analysis) is displayed in the upper-left panels.

At day 5 (Fig. 6) the model forecasts still resemble the analysis, and the differences between the forecasts are small. Regions where the models do poorly (or well) tend to coincide. Low pressure over the Pacific Ocean (at about 50°N, 170°W) and also off the coast of Africa are not forecast well by the models; however, the position of the North American trough–ridge system appears relatively good. The strength of the flow across the top of this ridge in the vicinity of the pole is a good indication that the polar filtering scheme is working adequately in both the sigma and eta coordinate versions.

At day 10 (Fig. 7) the model forecasts have lost most of their resemblance to the analysis. The similarity between the gridpoint model forecasts is greater than between the gridpoint and spectral model forecasts. From the appearance of the gridpoint fields, stability in the polar region is not a problem at this time of the forecast. Longer integrations have also confirmed the stability of the gridpoint solutions.

To objectively assess the predictive skill of the models, anomaly correlation coefficients were computed for 500-mb height forecasts every 12 h out to 10 days. Figure 8a shows the anomaly correlation coefficients averaged for the four January cases of the E45 gridpoint models and the spectral model for the region from 20° to 80°N. Similar results at the E60 resolution are shown in Fig. 8b. Above the 0.6 reference line the apparent skill of the forecasts is similar; however, the spectral model scores (solid line) do appear slightly better than either E45 gridpoint model. When increasing the resolution of the gridpoint models to E60 this difference in the scores no longer exists. The lower E45 scores may be due to truncation error in the second-order differencing schemes. Comparing gridpoint models at the E45 resolution, the sigma coordinate correlation coefficients are slightly higher than for the eta coordinate. At the E60 resolution the difference in scores between vertical coordinates is negligible.

Although the predictive skill of each of the four cases varies (not shown), the relative performance of the models to each other is similar for all cases to that in

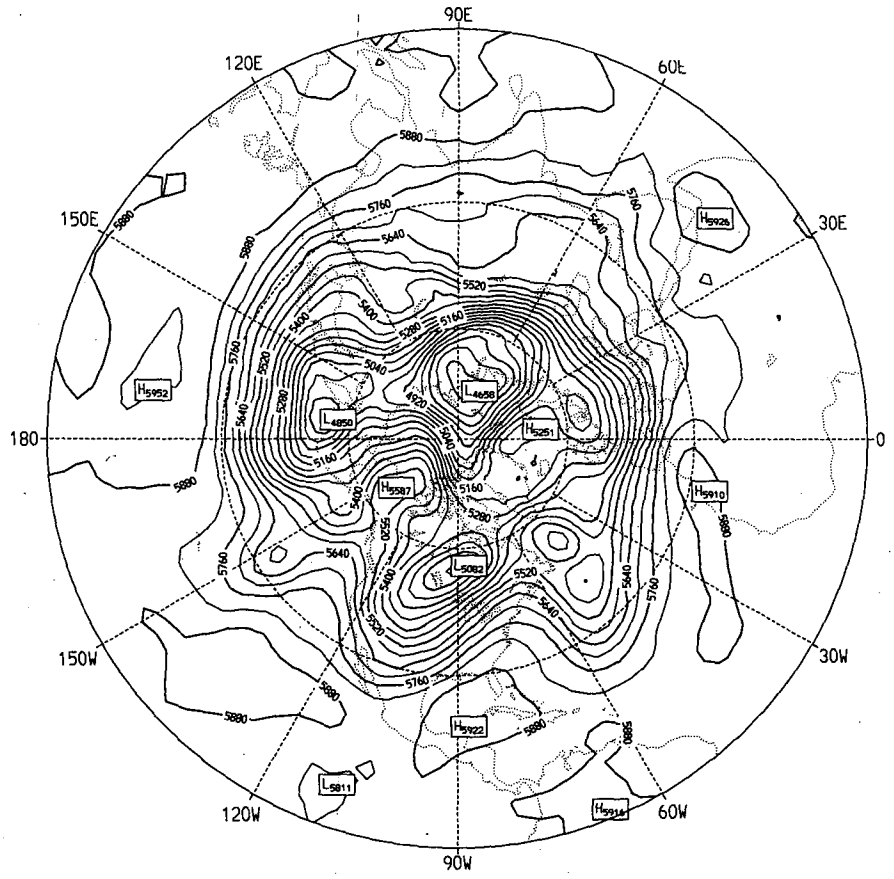

FIG. 5. Northern Hemisphere polar stereographic map of 500-mb height used as the initial condition for 0000 UTC 1 January 1979. Contour interval is 60 m.

Fig. 8. The higher-resolution gridpoint models consistently showed improvement in skill relative to their lower-resolution counterparts; this was especially true for the eta coordinate where all cases showed improvement. The spectral model scores were superior to the GEM for only one case; for other cases the level of performance was slightly lower than the gridpoint models.

The large-scale circulation produced by all the models is similar out to 10 days. Although the circulation produced by the spectral and GEM sigma models differs more than between the GEM sigma and eta models, the level of predictive skill is similar among all the models. It should be expected that at the relatively coarse resolution of the global model this type of large-scale validation may not reveal the strengths or weaknesses of the eta system. Important differences between the coordinates that are isolated near steep topography or close to the earth's surface have probably been lost by the spatial and temporal averaging of the verification.

A more regional examination of the flow above topography should reveal the advantages of the eta coordinate. Over steep topography the slope of the sigma coordinate surfaces can lead to numerical errors in the calculation of various quantities. While the pressure gradient force has been a well-documented example of this type of error, many other terms may also present problems. Simmons (1987) demonstrated inaccuracies associated with the calculation of advection and lateral diffusion terms along sloping sigma surfaces. The calculation of omega, from the omega-alpha term in (5b), also suffers from this problem; it is the sum of a vertical and horizontal contribution. In the eta model, the vertical term is much greater than the horizontal term, while in the sigma model both terms are of comparable magnitude and may have opposite signs. The resulting small value of omega in the sigma model may contain numerical errors similar to those documented for the pressure gradient and advection terms.

At the E45 resolution, Fig. 9 displays cross sections of the omega-alpha term through the Andes along the 20°S latitude circle. To minimize the impact of initial condition imbalances, the data has been averaged for days 5–10 from forecasts initialized at 0000 UTC 1 January 1979. The sigma coordinate solution (a) displays a noisier pattern over the steep topography, while away from the Andes the sigma and eta (b) solutions

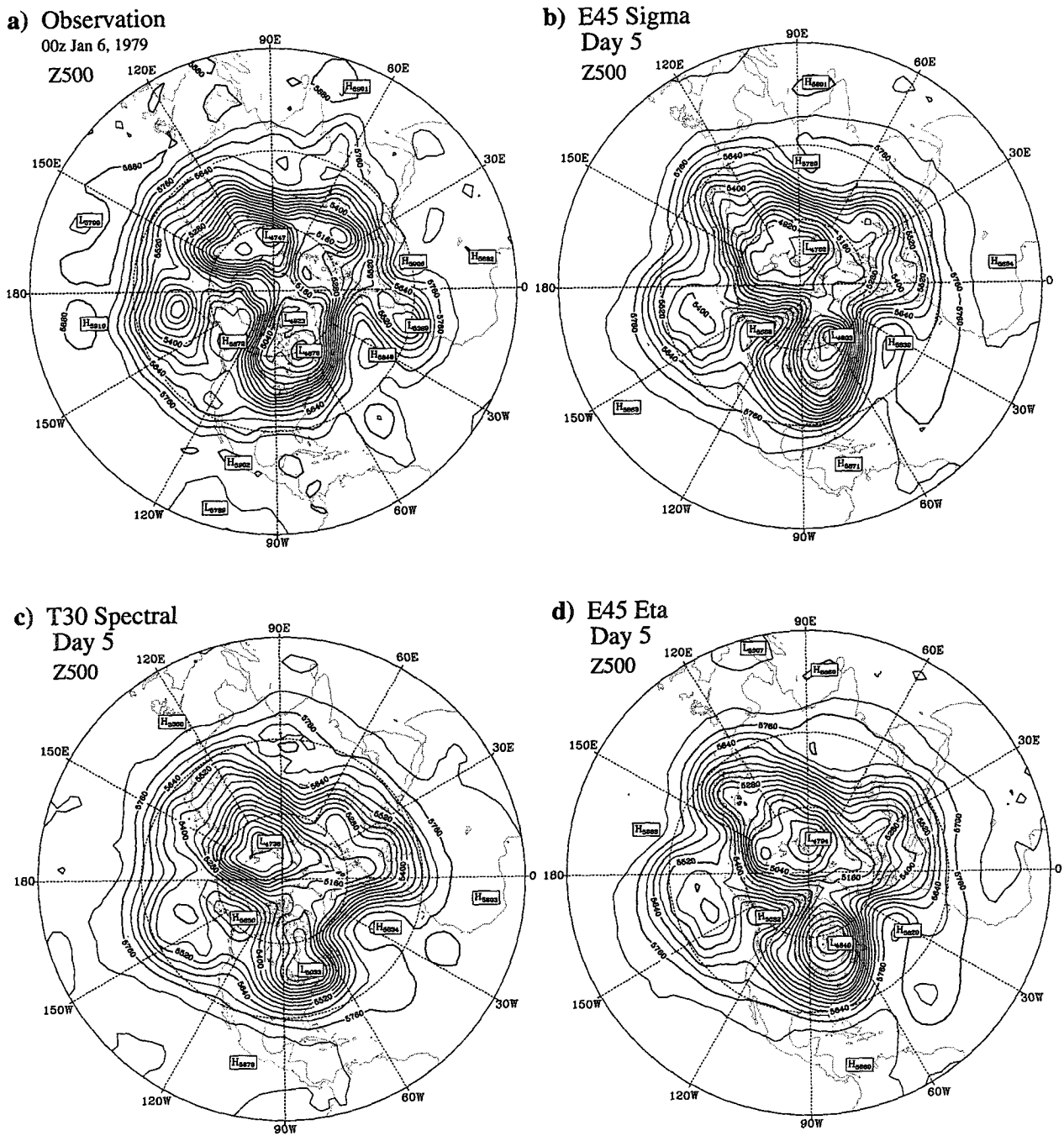

FIG. 6. Five-day forecast of 500-mb height valid 0000 UTC 6 January 1979. The Northern Hemisphere polar stereographic projections are for (a) NMC analysis, (b) sigma coordinate E45 GEM, (c) sigma coordinate T30 spectral model, and (d) eta coordinate E45 GEM. Contour interval is 60 m.

are similar. If the steepness of the topography is better resolved (i.e., horizontal resolution is increased), the sigma problem over steep topography should worsen (Mesinger 1982). At the E60 resolution, analogous cross sections (except at 21°S) are displayed in Fig. 10. Again the sigma solution (a) produces a noisier pattern over the Andes that is unrealistic and larger than at the lower resolution, while the eta solution (b) is again relatively free of distortion. While these numerical errors in the alpha-omega term will no doubt affect the quality and regional distribution of precipitation, the effect on the larger-scale circulation is not as obvious.

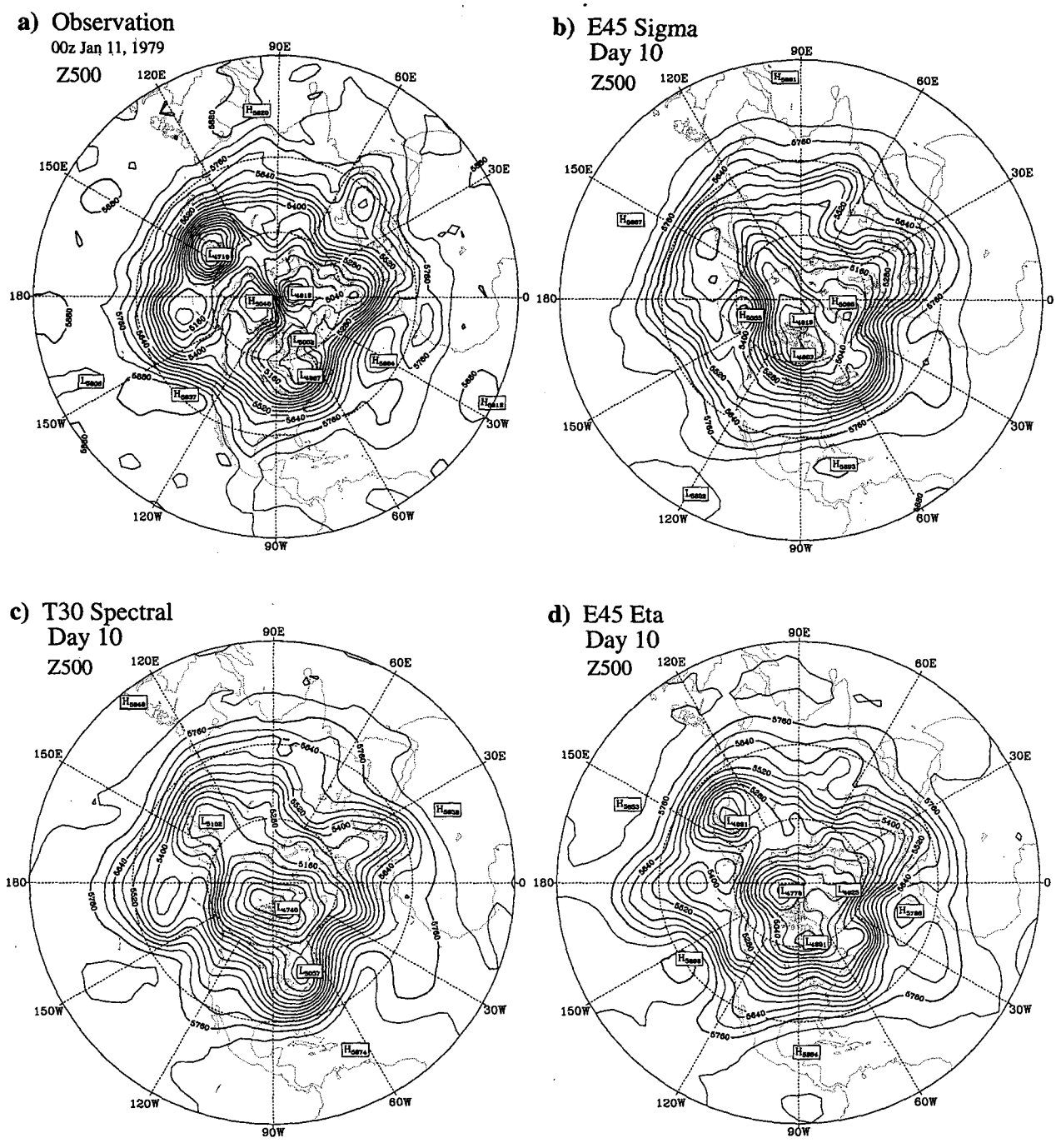

FIG. 7. Same as Fig. 6 except for a 10-day forecast valid 0000 UTC 11 January 1979.

A potential weakness of the eta coordinate may occur when the depth of the model's lowest atmospheric level becomes too large for the valid calculation of surface-layer turbulent fluxes. At grid points that have even modest elevation the depth of the model layer nearest the earth's surface is considerably greater for the eta coordinate. Over the highest elevations the eta surface-layer depth becomes even greater. The calculation of turbulent fluxes for these deep eta coordinate surface layers may result in large discrepancies with the sigma version. It is assumed that the uniform higher vertical resolution near the earth's surface in the sigma coordinate produces a solution that is more correct. The comparison of the surface fluxes and wind stress may

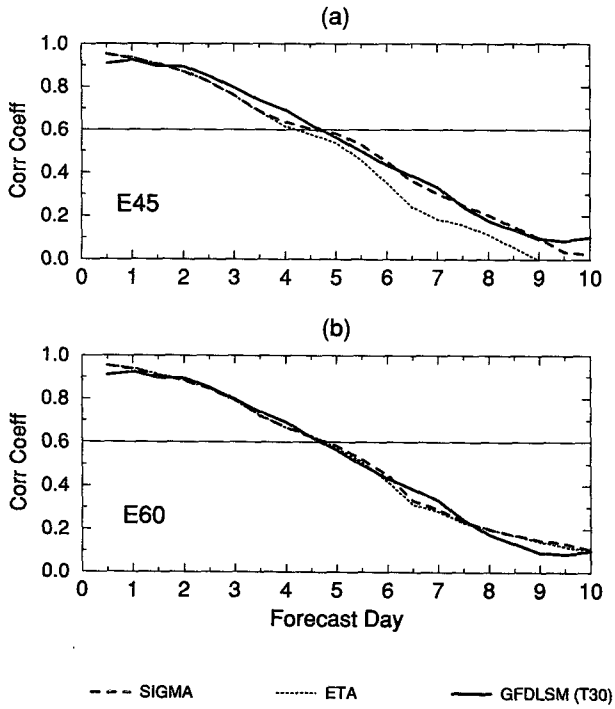

FIG. 8. Anomaly correlation for various model forecasts with the analysis of 500-mb height in the region 20°–80°N. The models are the GEM sigma (dashed line), GEM eta (dotted line), and the T30 GFDL spectral model (solid line): (a) GEM at the E45 resolution and (b) at the E60 resolution. A horizontal reference line indicates the 0.6 correlation.

provide some insight into the potential weaknesses of the surface-layer parameterization for the deeper eta coordinate layers.

The surface wind stress is a good quantity for comparison since it has no dependence on variables located at the earth's surface. The sensible and latent heat fluxes both rely on the surface temperature, which itself is a function of several quantities. Figure 11 displays the globally averaged surface wind stress of the eta coordinate normalized by the global average of the sigma coordinate. In Fig. 11a this ratio is displayed as averages for land points (over step topography), ocean points (no topography), and all points (globally). In Fig. 11b the averages for land points are separated further by the depth of the eta coordinate surface layer. There appears to be an obvious relationship between the depth of the surface layer and the underestimation of the wind stress. The global average indicates a 10%–20% deficiency in the eta coordinate stress over step topography, and over the deeper surface layers this deficiency becomes even larger.

The comparison of surface wind stress suggests that the deeper eta coordinate layers above elevated terrain underestimate the surface-layer mixing coefficients (and similarly the drag coefficient). The sensible and latent heat fluxes are directly affected by the mixing coefficients but the relationship is more complex because they also depend on the surface temperature. If a simple surface heat balance is solved assuming a temperature for the lowest model level and surface radiative flux (net solar plus downward longwave), the relationship between the surface temperature and drag coefficient (C_D) can be determined. Using a temperature of 273 K for the lowest atmospheric level, Fig. 12 shows this relationship for several values of surface radiation. Assuming a small (negative) error occurs in the eta coordinate drag coefficient, a much larger error results in the surface temperature when the drag is small. Small drag coefficients would typically correspond with a stable atmosphere. On the other hand, if the radiation is large, an underestimation of the drag results in a positive surface temperature error, and for low radiation the error results in colder surface temperatures. The global average value of surface radiation (about 500 W m^{-2}) indicates that a deficiency in the eta coordinate drag coefficient would result in a warmer surface temperature (globally) than the sigma model. Regionally, the higher latitudes with relatively low radiation in winter should have a colder temperature, especially for very stable conditions over snow or ice. In fact, over Greenland the eta model does have a colder surface temperature than the GEM sigma model.

Figure 13 shows the difference (eta minus sigma) of the globally averaged surface temperature for all land points and for different eta coordinate surface-layer depths. The eta coordinate temperature is consistently higher than that of the sigma coordinate. There also appears to be a relationship between the depth of the eta coordinate surface layer and the magnitude of the temperature difference. The largest differences occur over the deep (432 m) eta coordinate surface layers, while layers not as deep have smaller positive biases. Except for spinup effects in the first day, the global bias appears to increase with time (about 0.55° at day 10). Longer integrations have revealed that this systematic difference stabilizes at slightly more than 1.0° warmer for the eta coordinate. However, due to the possible sign reversal of the error (in Fig. 12), these biases probably do not reflect the actual magnitude of the error.

The warmer eta coordinate surface has a major role in influencing the latent and sensible heat fluxes. The relatively warmer surface increases the latent heat flux (by increasing the surface specific humidity) and offsets the effect of the weaker mixing coefficients. As a result, latent heat fluxes for the eta coordinate are actually larger than for the sigma coordinate. The sensible heat flux does not display an obvious weakening (or strengthening) in the deeper layers; the relationship is more complicated due to a possible sign reversal.

The impact of the relatively deep eta coordinate surface layers appears to be most significant for the prediction of surface temperature. The surface heat balance is quite sensitive for very stable conditions (and

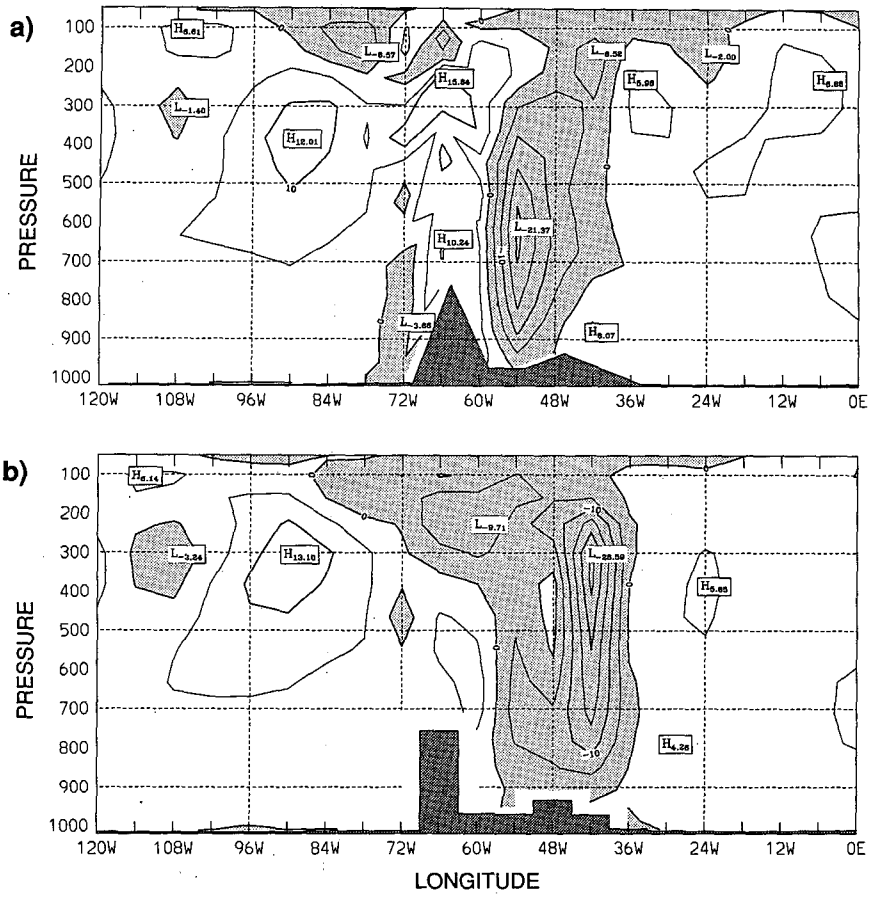

FIG. 9. Cross section of the omega-alpha term through the Andes at 20°S. Data for the E45 GEM (a) sigma and (b) eta models is averaged for days 5–10 from forecasts initialized at 0000 UTC 1 January 1979. Contour interval is 5 K day^{-1}. Negative values (rising motion) are shaded.

low wind speeds) where small errors in the strength of surface-layer mixing coefficients can cause large errors in the surface temperature. The impact on the lowest model level may not be as great. The examination of model atmospheres near the earth's surface do not show large differences between the eta and sigma coordinate. This may in part be due to the fact that the deep eta coordinate surface layers directly affect only roughly one-third of all grid points (i.e., land points), while the largest biases occurring over the deepest surface layers comprise a much small percentage of the earth's surface.

5. Concluding comments

A complete GCM has been developed using the Arakawa E grid and the eta vertical coordinate. Dynamics of the model have been adapted from the regional NMC eta model. Appropriate numerical techniques were applied in the polar region of the E-grid model so as to properly handle cross-polar flow. The physical parameterizations were made to conform with the GFDL E4 physics package. A unique feature of this model is a switch that allows the model to run using either the eta or sigma vertical coordinate and allows for a clean comparison of vertical coordinates. Comparisons have also been made with the GFDL Experimental Prediction Group spectral model. All models have been run with the same physical parameterizations.

Objectives have been to develop a gridpoint GCM with comparable skill to an established spectral GCM and to assess the worthiness of the eta coordinate relative to the sigma system in a global model. Validation of the models has focused on forecasts out to 10 days. Four January cases were run with two horizontal resolutions of the gridpoint models. As a measure of forecast skill, 500-mb heights and average anomaly correlations for the Northern Hemisphere were compared. Due to the limited ability of the anomaly correlations to demonstrate the advantages or disadvantages of the relatively isolated effects of a particular coordinate, additional analyses were performed near steep to-

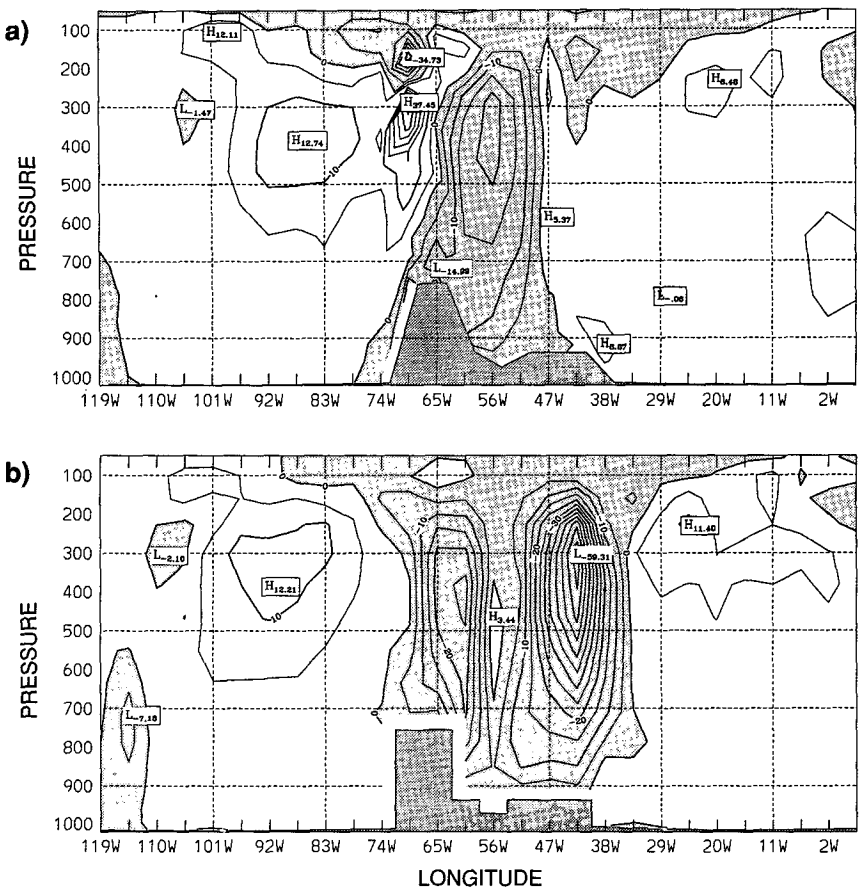

FIG. 10. Same as Fig. 9 except through the Andes at 21°S and for the E60 GEM.

pography and for the surface layer above elevated land points.

The GEM appears to produce reasonable forecasts when compared to the spectral model. Correlation coefficients of forecasted 500-mb heights in middle and high latitudes are in close agreement between all models. However, spectral model forecasts show a small increase in skill over the lower (E45) resolution gridpoint models. This may be due to truncation error in the second-order differencing schemes of the GEM. At the E60 resolution, the difference in skill scores of all models was negligible.

The nearly identical computer codes used by the GEM sigma and eta models produced very similar forecasts out to 10 days. The eta coordinate shows no deficiency in polar regions relative to the GEM sigma or the spectral model. The polar filtering scheme for the E grid and the eta coordinate appears to be performing adequately. Similarly, correlation coefficients of forecasted 500-mb heights were remarkably close. At the E45 resolution, the forecast skill of the GEM sigma version was slightly better than for the eta coordinate; this difference disappeared at the E60 resolution.

With higher horizontal resolution, the topography will be better resolved and the mountains (and sigma surfaces) will be steeper (Mesinger 1982). Cross sections of omega-alpha through the Andes provided an example of the numerical problems steep sigma surfaces can produce. As horizontal (and vertical) resolution increases, these types of problems can degrade the anticipated improvements in model performance of the sigma coordinate but not for the eta model.

The lack of vertical resolution in the surface layer presents the most challenging problem for the eta coordinate. Monin–Obukhov similarity theory was applied for this layer. An examination of surface wind stress revealed that the deeper eta coordinate surface layers were underestimating the mixing coefficients by 10%–20%. The impact of this deficiency appeared greatest on surface temperatures beneath the deepest eta coordinate surface layers, where globally a higher temperature was produced. The direct impact of the reduced mixing coefficients on other quantities of the eta model was not as great. Although the eta coordinate produced results in the surface layer that differ from

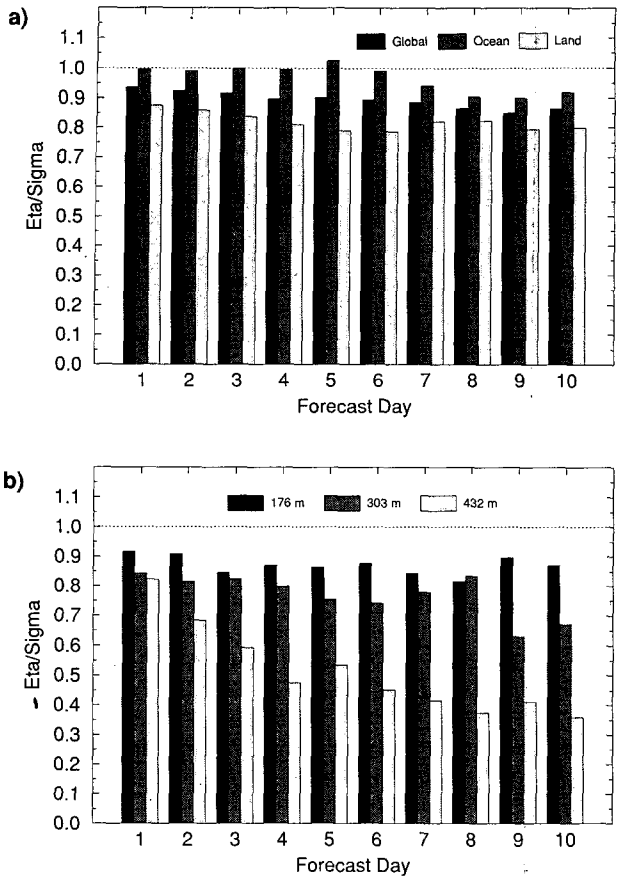

FIG. 11. Globally averaged surface wind stress for the eta coordinate normalized by the sigma coordinate average. Forecasts were initialized at 0000 UTC 1 January 1979. Panel (a) displays averages globally (at all points), at ocean points (no step topography), and at land points (with step topography). Panel (b) displays averages at land points for several depths of the eta coordinate surface layer.

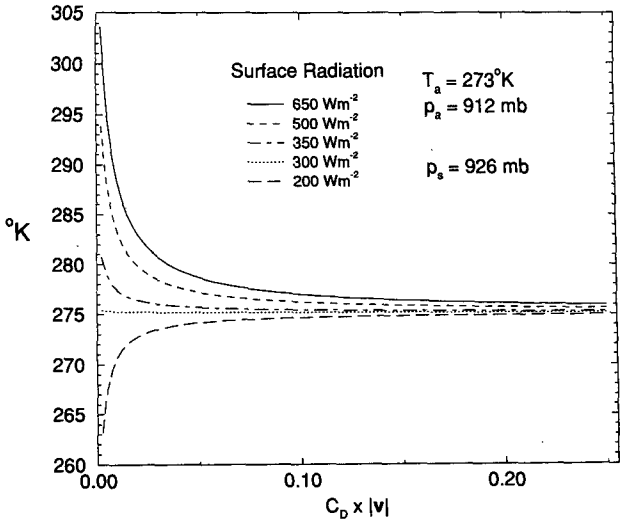

FIG. 12. Surface temperature as a function of mixing coefficient (drag coefficient times wind speed) for several values of surface radiation. Derived from the surface heat balance assuming atmospheric variables at the lowest model level (T_a = 273 K and p_a = 912 mb) and surface (p_s = 926 mb).

the sigma solution, both are usable for extended-range and climate prediction.

Perhaps the largest benefit of the model presented is its ability to compare two different vertical coordinates within the same GCM framework. An unbiased comparison of the eta and sigma vertical coordinates should be designed to minimize differences in the physical parameterizations so that the advantages (or disadvantages) of the coordinates can be observed. Although the eta coordinate did not display significant improvements over the sigma coordinate, the result is considered positive. It attests to the reliability of the development and incorporation of the physical parameterizations into the eta model.

Acknowledgments. The development of this model involved the help of many very generous individuals. First and foremost, the author thanks Drs. Fedor Mesinger and Zaviša Janjić, at the National Meteorological Center, for the use of their regional model and assistance with many important issues. The author is also grateful to Dr. Miodrag Rančić for his assistance with the polar problems, and Mr. Thomas Black for answering many questions about the model.

The author especially thanks Dr. Kikuro Miyakoda for his guidance and support throughout the long, tedious process of model development. The author is grateful to the following people at the Geophysical Fluid Dynamics Laboratory: Mr. William Stern for his assistance with the spectral model integrations, Mr. Joseph Sirutis for answering questions regarding the E4 physical parameterizations, Mr. Daniel Schwarzkopf for helping to incorporate the radiative algorithms into

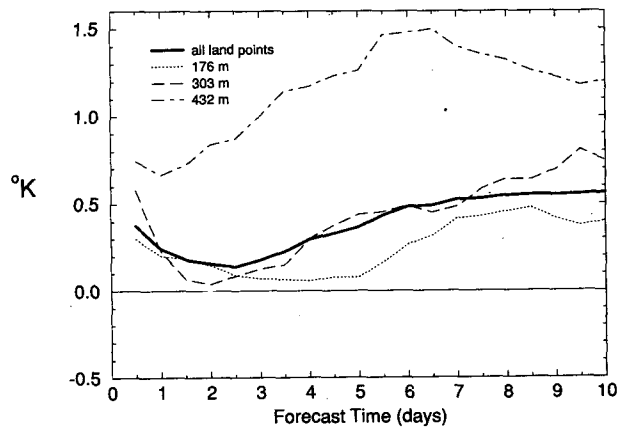

FIG. 13. Surface temperature difference (eta minus sigma) at all land points and over three depths of the eta coordinate surface layer averaged globally for all four cases of the E45 GEM.

the eta model; Dr. Jeffrey Anderson for his reviews of the manuscript and helpful comments, and Dr. Brian Gross and Mr. Robert Tuleya for their reviews of the manuscript. In addition, the author thanks three anonymous reviewers for their comments that helped to improve the manuscript.

APPENDIX

Cross-Polar Flow Experiments

A series of integrations were performed with the shallow-water equations to test the polar boundary treatment and numerical schemes of the model. The numerics of the global model should conserve the quantities they were designed to conserve in the interior of the regional model. The polar boundary should allow cross-polar flow that is free from distortion. For this purpose Rossby–Haurwitz wavenumber 1 fields (Phillips 1959) were used as the initial condition. Figure A1 shows the initial height field (at the E45 resolution) used for all wavenumber 1 experiments. Tests performed without polar filtering were run with a sufficiently short time step to guarantee computational stability in polar regions. Of particular interest was the effect of the divergence modification for preventing the grid separation problem and the stability of this term in polar regions. Additional tests were made with the proposed polar filtering scheme so that a longer time step could be used.

The numerical schemes are designed to conserve mass (or height for the shallow water equations), total energy, and momentum (Janjić 1984; Rančić and Ničković 1988). Mesinger's divergence modification is designed to conserve only mass, for the shallow-water equations total energy is not conserved. Total energy is defined as the sum of kinetic plus the active part of available potential energy [see Rančić and Ničković, Eqs. (26), (39), and (40)]. In addition, the polar filtering scheme (as applied to time tendencies) does not conserve energy (Takacs and Balgovind 1983). Total energy conservation (or lack of it) for the shallow-water equations will be demonstrated.

The shallow-water equations were integrated with a time-differencing scheme identical to that used by the GCM described in section 3. For the experiments without polar filtering the time step for the adjustment process was 30 s at the E45 resolution and 15 s for the E60 model. In runs with polar filtering this time step

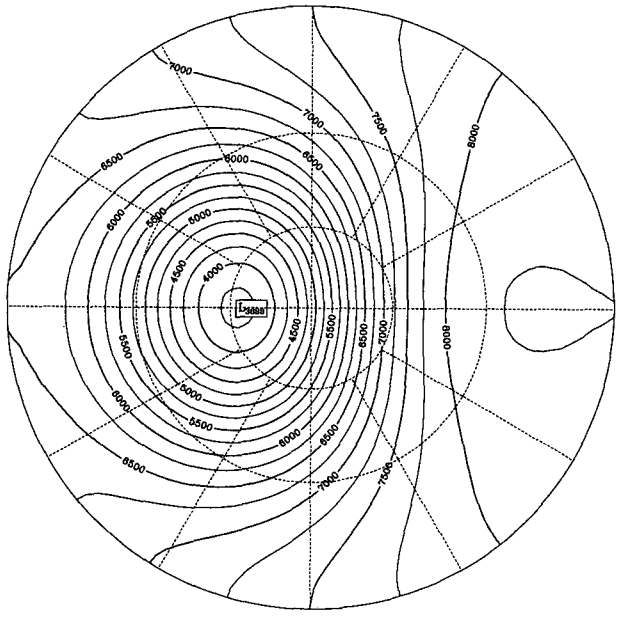

FIG. A1. Hemispheric stereographic projection of initial Rossby–Haurwitz wavenumber 1 height field used for integration of the shallow-water equations. Contour interval is 250 m.

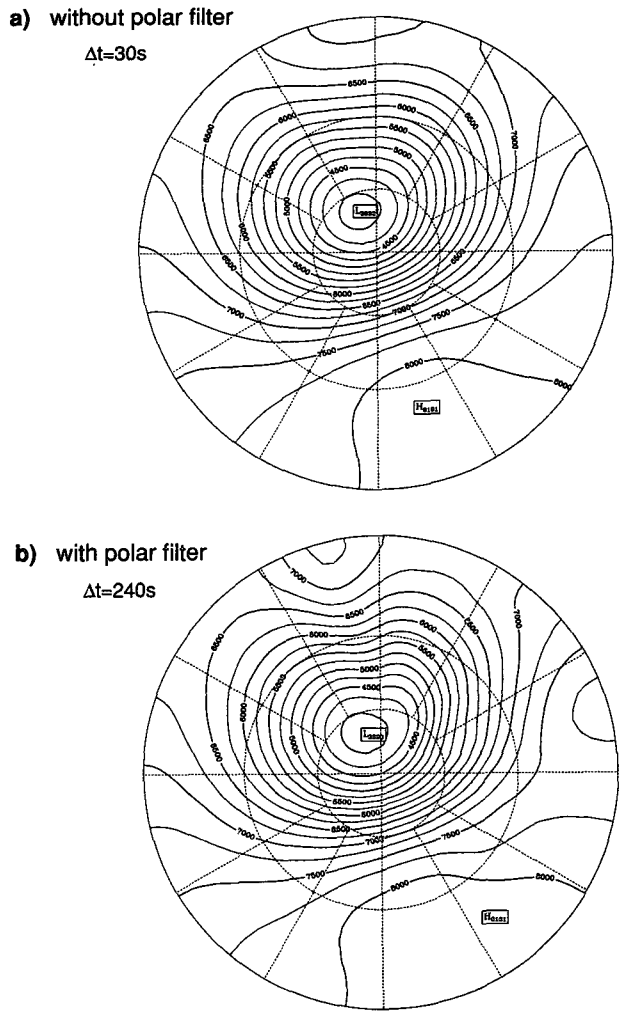

FIG. A2. Height after 10-day integration with shallow-water equations. Integrations were run (a) without polar filtering and (b) with polar filtering; both used the divergence modification. Initial condition is shown in Fig. A1. Contour interval is 250 m.

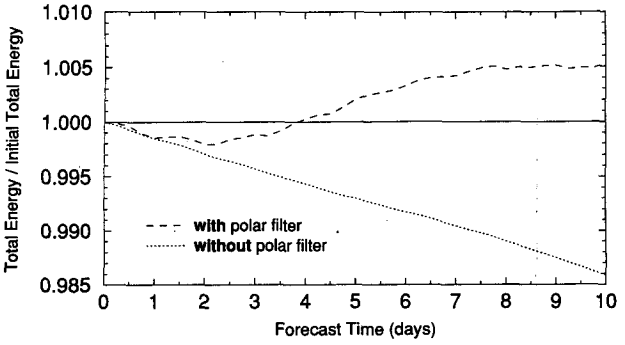

FIG. A3. Globally averaged total energy normalized by the initial value as a function of forecast day corresponding to the integrations shown in Fig. A2.

was 240 and 120 s for the E45 and E60 models, respectively. For brevity, only the results at the E45 resolution are presented here, nearly identical results were produced by the E60 model.

Figure A2 shows the height field at day 10 for experiments without the polar filtering scheme (panel a) and with polar filtering (panel b). Both runs use the divergence modification to suppress the grid separation problem but included no other type of diffusion. The run without polar filtering (a) shows the flow across the pole is for the most part free of distortion and the wavenumber 1 field has not changed shape significantly from the initial time (Fig. A1). The experiments with the proposed polar filtering scheme (b) when compared to (a) display little change in the shape, position, or intensity of the cross-polar flow.

Figure A3 displays the evolution of globally averaged total energy (normalized by the initial value) for the experiments with and without polar filtering. Without polar filtering the lack of energy conservation for the divergence modification term can be seen in the downward trend of total energy (lower curve in Fig. A3). Longer integrations have shown this downward trend to continue until the model becomes unstable. Integrations without the divergence modification (or polar filtering) have not displayed this sort of energy loss. When polar filtering is used the downward trend in total energy does not exist (upper curve in Fig. A3). The longer time step has generated this additional energy in small-scale unstable waves. The polar filtering scheme appears to be suppressing enough of the small-scale energy for the solution to remain stable. The change in total energy over the 10-day integrations is relatively small (0.5%) and as confirmed by longer integrations has reached an equilibrium.

REFERENCES

Arakawa, A., 1966: Computational design for long-term numerical integration of the equations of fluid motion: Two-dimensional incompressible flow. Part I. *J. Comput. Phys.*, **1**, 119–143.

——, and V. R. Lamb, 1977: Computational design of the basic dynamical processes of the UCLA general circulation model. *Methods in Computational Physics,* Vol. 17, J. Chang, Ed., Academic Press, 173–265.

——, and M. J. Suarez, 1983: Vertical differencing of the primitive equations in sigma coordinates. *Mon. Wea. Rev.*, **111**, 34–45.

Corby, G. A., A. Gilchrist, and R. L. Newson, 1972: A general circulation model of the atmosphere suitable for long period integrations. *Quart. J. Roy. Meteor. Soc.*, **98**, 809–832.

Delsol, F., K. Miyakoda, and R. H. Clarke, 1971: Parameterized processes in the surface boundary layer of an atmospheric circulation model. *Quart. J. Roy. Meteor. Soc.*, **97**, 181–208.

Fels, S. B., and M. D. Schwarzkopf, 1975: The simplified exchange approximation: A new method for radiative transfer calculations. *J. Atmos. Sci.*, **32**, 1476–1488.

——, and ——, 1981: An efficient, accurate algorithm for calculating CO_2 15-μm band cooling rates. *J. Geophys. Res.*, **86**(C2), 1205–1232.

Gadd, A. J., 1978: A split explicit integration scheme for numerical weather prediction. *Quart. J. Roy. Meteor. Soc.*, **104**, 569–582.

Gates, W. L., 1992: An AMS continuing series: Global change, AMIP: The atmospheric model intercomparison project. *Bull. Amer. Meteor. Soc.*, **73**, 1962–1970.

Gordon, C. T., and W. F. Stern, 1982: A description of the GFDL global spectral model. *Mon. Wea. Rev.*, **110**, 625–644.

——, and ——, 1984: Medium range prediction by a GFDL global spectral model: Results for three winter cases and sensitivity to dissipation. *Mon. Wea. Rev.*, **112**, 217–245.

Janjić, Z. I., 1977: Pressure gradient force and advection scheme used for forecasting with steep and small scale topography. *Contrib. Atmos. Phys.*, **50**, 186–199.

——, 1979: Forward-backward scheme modified to prevent two-grid-interval noise and its application in sigma coordinate models. *Contrib. Atmos. Phys.*, **52**, 69–84.

——, 1984: Nonlinear advection schemes and energy cascade on semi-staggered grids. *Mon. Wea. Rev.*, **112**, 1234–1245.

——, 1990: The step-mountain coordinate: Physical package. *Mon. Wea. Rev.*, **118**, 1429–1443.

——, and F. Mesinger, 1984: Finite difference methods for the shallow water quations on various horizontal grids. *ECMWF Seminar 1983, Numerical Methods for Weather Prediction,* Shinfield Park, Reading, United Kingdom, ECMWF, 29–101.

——, ——, and T. L. Black, 1988: Horizontal discretization and forcing. *Workshop on Techniques for the Horizontal Discretization in Numerical Weather Prediction Models,* Shinfield Park, Reading, United Kingdom, ECMWF, 207–227.

Kurihara, Y., 1965: On the use of implicit and iterative methods for the time integration of the wave equation. *Mon. Wea. Rev.*, **93**, 33–46.

——, and G. J. Tripoli, 1976: An iterative time integration scheme designed to preserve a low-frequency wave. *Mon. Wea. Rev.*, **104**, 761–764.

Manabe, S., 1969: Climate and the ocean circulation. Part 1: The atmospheric circulation and the hydrology of the earth's surface. *Mon. Wea. Rev.*, **97**, 739–774.

——, J. Smagorinsky, and R. F. Strickler, 1965: Simulated climatology of a general circulation model with a hydrologic cycle. *Mon. Wea. Rev.*, **93**, 769–798.

Matsuno, T., 1966: Numerical integrations of the primitive equations by a simulated backward difference method. *J. Meteor. Soc. Japan*, **44**, 76–84.

Mellor, G. L., and T. Yamada, 1982: Development of a turbulence closure model for geophysical fluid problems. *Rev. Geophys. Space Phys.*, **20**, 851–875.

Mesinger, F., 1973: A method for construction of second-order accuracy difference schemes permitting no false two-grid interval wave in the height field. *Tellus*, **25**, 444–458.

——, 1977: Forward–backward scheme, and its use in a limited area model. *Contrib. Atmos. Phys.*, **50**, 186–199.

——, 1981: Horizontal advection schemes of a staggered grid—An enstrophy and energy-conserving model. *Mon. Wea. Rev.*, **109,** 467–478.

——, 1982: On the convergence and error problems of the calculation of the pressure gradient force in sigma coordinate models. *Geophys. Astrophys. Fluid Dyn.*, **19,** 105–117.

——, 1984: A blocking technique for representation of mountains in atmospheric models. *Riv. Meteor. Aeronautica,* **44,** 195–202.

——, and Z. I. Janjić, 1987: Numerical techniques for the representation of mountains. *Observation, Theory and Modelling of Orographic Effects,* Seminar/Workshop, Shinefield Park, Reading, United Kingdom, ECMWF, 29–80.

——, and T. L. Black, 1992: On the impact on forecast accuracy of the step-mountain (eta) vs. sigma coordinate. *Meteor. Atmos. Phys.*, **50,** 47–60.

——, Z. I. Janjić, S. Ničković, D. Gavrilov, and D. G. Deaven, 1988: The step-mountain coordinate: Model description and performance for cases of Alpine lee cyclogenesis and for a case of an Appalachian redevelopment. *Mon. Wea. Rev.*, **116,** 1493–1518.

Miyakoda, K., and J. Sirutis, 1977: Comparative integrations of global models with various parameterized processes of subgrid-scale vertical transports: Description of the parameterizations. *Contrib. Atmos. Phys.*, **50,** 445–487.

Phillips, N. A., 1957: A coordinate system having some special advantages for numerical forecasting. *J. Meteor.*, **14,** 184–185.

——, 1959: Numerical integration of the primitive equations on the hemisphere. *Mon. Wea. Rev.*, **87,** 333–345.

Pierrehumbert, R. T., 1987: An essay on the parameterization of orographic gravity wave drag. *Observation, Theory and Modelling of Orographic Effects,* Seminar/workshop, Shinfield Park, Reading, United Kingdom, ECMWF, 251–282.

Rančić, M., and S. Ničković, 1988: Numerical testing of E-grid horizontal advection schemes on the hemisphere. *Contrib. Atmos. Phys.*, **61,** 265–273.

Schwarzkopf, M. D., and S. B. Fels, 1991: The simplified exchange method revisited: An accurate, rapid method for computation of infrared cooling rates and fluxes. *J. Geophys. Res.*, **96**(D5), 9075–9096.

Shapiro, R., 1970: Smoothing, filtering, and boundary effects. *Rev. Geophys. Space Phys.*, **8,** 359–387.

Simmons, A. J., 1987: Orography and development of the ECMWF forecast model. *Observation, Theory and Modelling of Orographic Effects,* Seminar/Workshop, Shinefield Park, Reading, United Kingdom, ECMWF, 129–163.

——, 1988: Some aspects of the design and performance of the global ECMWF spectral model. *Workshop on Techniques for the Horizontal Discretization in Numerical Weather Prediction Models,* Shinefield Park, Reading, United Kingdom, ECMWF, 249–303.

——, and M. Jarraud, 1984: The design and performance of the new ECMWF operation model. *ECMWF Seminar 1983, Numerical Methods for Weather Prediction,* Shinefield Park, Reading, ECMWF, 113–164.

Sirutis, J., and K. Miyakoda, 1990: Subgrid scale physics in 1-month forecasts. Part I: Experiment with four parameterization packages. *Mon. Wea. Rev.*, **118,** 1043–1064.

Smagorinsky, J., 1963: General circulation experiments with the primitive equations. Part I: The basic experiment. *Mon. Wea. Rev.*, **91,** 99–164.

Stern, W. F., and R. T. Pierrehumbert, 1988: The impact of an orographic gravity wave drag parameterization on extended range predictions with a GCM. Preprints, *Eighth Conf. on Numerical Weather Prediction,* Baltimore, MD, Amer. Meteor. Soc., 745–750.

Takacs, L. L., and R. C. Balgovind, 1983: High-latitude filtering in global grid-point models. *Mon. Wea. Rev.*, **111,** 2005–2015.

Tomine, K., and S. Abe, 1982: A trial to reduce truncation errors of the pressure gradient force in sigma coordinate systems. *J. Meteor. Soc. Japan,* **60,** 709–716.